Journal of Power Sources 185 (2008) 1056–1065

Contents lists available at ScienceDirect

Journal of Power Sources

journal homepage: www.elsevier.com/locate/jpowsour

Modeling efficiency and water balance in PEM fuel cell systems with liquid fuel processing and hydrogen membranes

Joshua B. Pearlman[a], Atul Bhargav[a], Eric B. Shields[a], Gregory S. Jackson[a,*], Patrick L. Hearn[b]

[a] Department of Mechanical Engineering, University of Maryland, College Park, MD 20742, USA
[b] Ballard Power Systems, Burnaby, British Columbia V5J 5J8, Canada

ARTICLE INFO

Article history:
Received 23 June 2008
Received in revised form 28 July 2008
Accepted 20 August 2008
Available online 29 August 2008

Keywords:
PEM fuel cell
Reforming
H_2 purification
Modeling

ABSTRACT

Integrating PEM fuel cells effectively with liquid hydrocarbon reforming requires careful system analysis to assess trade-offs associated with H_2 production, purification, and overall water balance. To this end, a model of a PEM fuel cell system integrated with an autothermal reformer for liquid hydrocarbon fuels (modeled as $C_{12}H_{23}$) and with H_2 purification in a water–gas-shift/membrane reactor is developed to do iterative calculations for mass, species, and energy balances at a component and system level. The model evaluates system efficiency with parasitic loads (from compressors, pumps, and cooling fans), system water balance, and component operating temperatures/pressures. Model results for a 5-kW fuel cell generator show that with state-of-the-art PEM fuel cell polarization curves, thermal efficiencies >30% can be achieved when power densities are low enough for operating voltages >0.72 V per cell. Efficiency can be increased by operating the reformer at steam-to-carbon ratios as high as constraints related to stable reactor temperatures allow. Decreasing ambient temperature improves system water balance and increases efficiency through parasitic load reduction. The baseline configuration studied herein sustained water balance for ambient temperatures $\leq$35 °C at full power and $\leq$44 °C at half power with efficiencies approaching ~27 and ~30%, respectively.

1. Introduction

While significant work has been done on modeling individual components of a PEM fuel cell system, integrated system simulation (including balance-of-plant) presents a challenge for the design of actual fuel cell power generators. This challenge for simulating balance-of-plant is substantially more complicated when liquid hydrocarbon fuel processing and subsequent H_2 purification must be incorporated into the analysis. The needs for recovering waste-heat and for sustaining water balance in both the fuel processor and fuel cell stack require significant thermal integration and mass flow recycling. Consequently, it is difficult to evaluate single component operation outside of the context of the entire system. Integrated system models must include the PEM fuel cell stack, the fuel processing system (with steam and/or air input), a hydrogen purification process, and the requisite balance-of-plant components (liquid pumps, compressors, heat exchangers, and cooling loops). Detailed component models with multi-dimensional grids, such as for PEM fuel cell stacks [1–5] and for catalytic fuel processors [6,7], become computationally prohibitive for integrated system-level analysis for a broad range of operating conditions and design modifications. As a result, integrated system models with lumped analysis for individual components [8–12] have been used for evaluating system design and feasibility of complex integrated PEM fuel cell power plants with hydrocarbon fuel processors.

Even simplified component level analyses for fuel cells with liquid hydrocarbon fuel processing show a wide-degree of variability in the detail of their approaches. Approaches for evaluating system water balance that include the fuel processor and PEM fuel cell have been presented for idealized fuel processors either without consideration of CO contamination in the fuel cell or with preferential oxidation reactors for CO clean-up [8,9]. The previous studies show the importance of exhaust water recovery for maintaining water balance, but these models presented in the literature have not fully incorporated the effects of fuel cell performance and balance-of-plant parasitic losses on overall water demand. Simulating the integrated performance of an autothermal fuel processor with a PEM fuel cell system requires proper accounting of the thermal integration for the fuel processor due to the wide variability in exothermicity/endothermicity of fuel processors with variations in steam to carbon (S/C) and oxygen to carbon (O/C) feed ratios. Studies from Argonne National Laboratory have focused

* Corresponding author. Tel.: +1 301 405 2368; fax: +1 301 405 2025.
E-mail address: gsjackso@umd.edu (G.S. Jackson).

0378-7753/$ – see front matter © 2008 Elsevier B.V. All rights reserved.
doi:10.1016/j.jpowsour.2008.08.057

Nomenclature

A_{cel}	geometric area of single electrochemical cell in fuel cell stack (cm^2)
$h_{H_2,comb}$	lower enthalpy of combustion of H_2 ($J\,kg^{-1}$)
$h_{HC,comb}$	lower enthalpy of combustion of hydrocarbon ($J\,kg^{-1}$)
i	average effective current density per unit area in the fuel cell stack ($A\,cm^{-2}$)
$\dot{m}_{H_2,mem}$	mass flow rate of H_2 out of low pressure side of the Pd-alloy-membrane ($kg\,s^{-1}$)
$\dot{m}_{HC,in}$	mass flow rate of hydrocarbon into fuel reformer ($kg\,s^{-1}$)
n_{cells}	number of electrochemical cells in fuel cell stack
O/C	oxygen (from O_2) to carbon (from fuel) atomic ratio in fuel reformer inlet
S/C	steam to carbon (from fuel) ratio in fuel reformer inlet
T_{amb}	ambient temperature (°C or K)
T_{exh}	exhaust condenser outlet temperature (°C or K)
V_{cell}	voltage across an individual electrochemical cell in stack (V)
$\dot{W}_{lost}$	parasitic power lost due to balance-of-plant components and dc–ac inverter (W)
$\dot{W}_{net}$	net electrical power out (W)

Greek Symbols

η_{BOP}	effective efficiency associated with power delivered to power produced by stack
η_{FC}	effective efficiency of fuel cell stack
η_{FP}	effective efficiency of fuel processor and Pd-alloy-membrane purifier combined
η_{th}	overall effective system efficiency

on liquid hydrocarbon reforming without H_2 purification [8] and with a preferential oxidation reactor for CO clean-up and an idealized reformate tolerant stack [10,12]. Other studies investigated a detailed model of a down-the-channel reformer with a Pd-based H_2 separation membrane [11], similar to what is considered in the present paper. Nonetheless, previous studies on liquid hydrocarbon processing did not fully address the impact of balance-of-plant on fuel processor loads, fuel cell power demand, and system temperatures, particularly for small portable power (<10 kW) applications which underlie the current study.

The current study attempts to extend the previously published analyses of integrated PEM fuel cell systems with liquid hydrocarbon fuel processors by performing mass and energy balances on a workable system that includes an integrated water–gas-shift reactor/H_2 palladium (Pd) alloy membrane separator to ensure reliable PEM performance. The present analysis is for an integrated system that produces between 0.5 and 5 kW net power out using a kerosene surrogate ($C_{12}H_{23}$ with thermodynamic properties defined previously [13]). By exploring the mass and energy balances of the fuel processor, H_2 purification, fuel cell system, and balance-of-plant, this model provides critical assessment not only of the important trade-offs in terms of thermal efficiency and water balance, but also of the necessary component performance requirements and range of operating conditions amenable for efficient and sustainable system operation. The following sections will present the system layout and modeling approach, followed by a discussion of simulation results on critical system performance trends for a range of operating conditions as well as component performance criteria.

2. System model

2.1. System configuration

A liquid-fuel processor and H_2 purification system can be integrated into a PEM fuel cell power generator in a number of possible flow configurations, each with different approaches to thermal and water management. System-level modeling, as presented in this study and earlier work [8,10,11], is needed to compare an array of possible configurations. Furthermore, assessing the viability and robustness of a particular design requires the determination of performance over a range of working conditions. The paper focuses on one particular configuration, illustrated in Fig. 1, that integrates a PEM fuel cell stack with a liquid fuel processor, a water–gas-shift/Pd membrane reactor for H_2 purification, and additional balance-of-plant subsystems.

The H_2 supply for the fuel cell anode is obtained from an autothermal fuel reformer, followed by a water–gas-shift reactor that is integrated with a Pd-alloy-membrane for H_2 separation. Because the fuel processor is upstream of the H_2 separation membrane, it must operate at sufficient pressure to provide a pressure differential (in this case, 6.0 barg) for driving H_2 across the membrane. The model assumes a desulfurized fuel source; and thus no pressure drop penalty for sulfur removal is incorporated in the fuel processor. Pumps for fuel and water, along with a high-pressure, low-flow-rate compressor for air, provide inlet flows to the fuel processor. On the low-pressure side of the Pd-alloy-membrane, purified H_2 is carried from the membrane by a flow of sweep steam. The sweep steam also acts as a diluent, reducing H_2 partial pressure and promoting diffusion across the membrane. The fraction of H_2 not diffusing across the membrane, along with all other reformate species, exits the membrane separator as retentate.

The H_2/H_2O mixture flow exiting the low-pressure side of the membrane separator cools as it mixes with H_2/water vapor recirculated from the anode exhaust, and this combined flow is further cooled through a heat exchanger before entering the anode. Part of the water vapor condenses in the heat exchanger and is available for re-use in the system. Additional liquid water is recovered from flow exiting the anode. Collected water that is needed for sweep steam is pumped to a steam generator and vaporized. Any surplus liquid water can be stored or sent to the fuel processor as required. Flow through the fuel cell anode is recirculated, ensuring uniform H_2 distribution and preventing liquid water accumulation along the anode channels while utilizing all available H_2. A compressor provides the pressure differential needed to induce flow recirculation through the anode. N_2 buildup in an anode recirculation due to leakage across the Nafion membrane will require some purging, and a recent study indicates that purging to maintain N_2 content below 1.5% costs the fuel cell stack efficiency approximately 1% [14]. Such a purge cycle is not readily modeled in a steady-state model and the small impact on overall efficiency in the system motivates the assumption in this study that the purge in the anode recirculation loop is negligible.

Air is supplied to the fuel cell cathode by a rotary vane compressor and is cooled through a heat exchanger after exiting the compressor. A gas-to-gas humidifier with a Nafion-based water membrane humidifies the air stream entering the cathode with water removed from the cathode exhaust.

Both retentate and cathode exhaust are fed to a catalytic burner. Burner exhaust provides heat input to the reformer pre-heater, reformer steam generator, and reformer fuel vaporizer. Further downstream, the exhaust is cooled in a condenser to recover water. The water thus recovered can be recycled to the fuel processor, but cannot be used for sweep steam or cathode humidification because

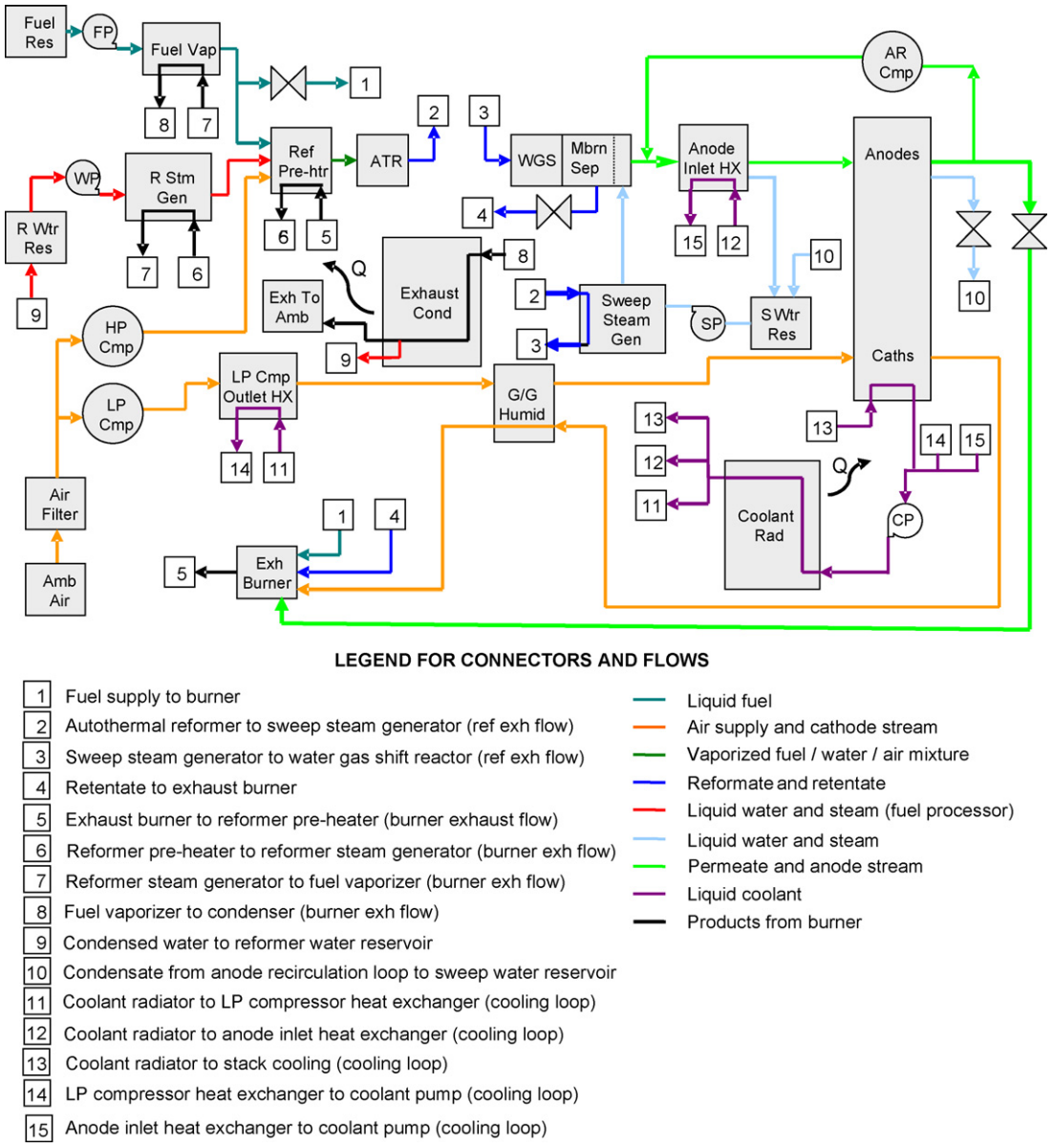

Fig. 1. Schematic diagram showing realization of PEM fuel cell system integrated with liquid fueled ATR reactor, water–gas-shift/Pd-alloy-membrane reactor, and retentate exhaust burner for waste-heat recovery.

of the presence of H_2CO_3 and other potential impurities that may impact long-term stability of the PEM fuel cell stack.

A liquid coolant loop removes heat from the fuel cell stack, in addition to cooling heat exchangers for the anode recirculation flow and cathode inlet flow. The coolant is circulated through a radiator, where the accumulated heat is rejected to the ambient.

2.2. System modeling approach

The model data is imported into MS Excel with a complex Visual Basic program running as a macro that determines steady-state operating conditions and system performance through a nested iterative sequence. The recycling of mass and heat flows, along with the feedback between system operating conditions and parasitic loads, requires such an iterative solution technique. A given iteration works by using current values for flow rates and parasitic power losses for the system to determine a new value for power produced by the fuel cell stack. This power demand is then used to recalculate fuel and air flows, thermal loads for cooling components, and associated parasitic loads (from compressors, pumps, and cooling fans) for system operation. Fuel flow rate to the system is determined iteratively through a species balance to satisfy H_2 demand from the Pd-alloy-membrane purifier. The new flow rates thus are used to update the parasitic loads, and gross power demand for the fuel cell stack is calculated from the sum of net (i.e., usable) power demand and the parasitic loads.

An iterative solution technique is used to determine temperatures in each component to satisfy entropy constraints and energy balances. Successively repeated iterations that solve species and energy balance equations are conducted until the following criteria were met. (1) The difference in overall gross power demand and fuel cell power produced are within 10^{-4} W. (2) The internal enthalpy balance for each component is within 10^{-3} W. (3) The molar balance for the fuel cell anode recirculation loop is within 10^{-9} gmol s^{-1}. The iterative solver thus provides a steady-state solution of flow conditions and also necessary parasitic loads from compressors

and pumps and fans for heat removal. This solution approach is similar in nature to the approach for a system-level model of a methane-fueled PEM fuel cell system studied earlier [10], although that system relied on CO clean-up in a preferential oxidation reactor rather than a Pd-alloy-membrane for H_2 purification.

Thermodynamic properties are calculated based on JANAF tables. Thermodynamics of a surrogate kerosene ($C_{12}H_{23}$) is used for the liquid fuel [15]. Liquid enthalpies are calculated by subtracting the heat of vaporization and subsequent sensible heat removal (based on a constant liquid C_P) from the gas-phase value.

2.3. Component model description

Most components as shown in Fig. 1 are simulated with zero-order thermodynamic models. Exceptions include the combined water–gas-shift/Pd-alloy-membrane reactor, which is simulated by a 1D flow model in order to assess the shift in H_2 driving force across the membrane as a function of length through the reactor. Models for critical heat exchangers (the exhaust condenser, coolant radiator, anode flow condenser, and air compressor outlet heat exchanger, all indicated in Fig. 1) utilize component geometry to determine power needs for fans and coolant pump associated with those heat exchange processes.

2.3.1. Fuel cell stack model

The fuel cell is modeled as an isothermal reactor with cell voltage, V_{cell}, versus current density, i (A cm^{-2}), defined by a polarization curve comparable to recently published data for a system based on Ballard Power Systems technology [13]. The open circuit voltage is shifted up or down based on changes in the Nernst potential with changes in reactant partial pressures and temperatures T_{fc}. Since the power demands for all cases examined in this study drive the fuel cell beyond the polarization activation region of the V_{cell}–i curve, a linear approximation of the V_{cell}–i curve satisfactorily represents the region of the polarization curve that defines the range of operation for the power conditions explored in this study. Isothermal operation of the fuel cell is assumed because the system model incorporates a coolant loop with variable flow rates controlled to maintain a near constant T_{fc} = 65 °C, which is a reasonable value for long-term durable operation of Nafion-based membrane electrode assemblies (MEA's). An energy balance is used to calculate the coolant flow load and the consequential pump and fan work required for the fuel cell radiator loop. The gas-to-gas humidifier, which recaptures humidity for the cathode inlet from the cathode exhaust, is assumed to be large enough to humidify the cathode inlet flow fully at its exhaust temperature from the humidifier.

For the fuel cell stack model, the water balance requires knowledge of where the water product is removed (either with the anode or cathode flows). Recent detailed two-phase flow MEA models in agreement with experiments have shown that the net fraction of product water which diffuses back across the Nafion membrane to the anode depends strongly on the membrane thickness, the H_2 stoichiometry in the anode, and the humidity ratio in the anode [5]. This net fraction is typically quite small or near zero, but for thin Nafion membranes characteristics of the stack modeled in this study, a slight diffusion toward the anode is expected if the anode is not fully humidified. In this study a net fraction of 15% product water back to the anode is used as a constant stack average value. This value has a minor impact on system efficiency and the net system water balance.

2.3.2. Fuel processor and H_2 membrane reactor models

Fuel conversion in the reformer takes place through reactions with both steam and O_2. Steam-to-carbon (S/C) and oxygen-to-carbon (O/C) ratios are user-specified inputs and set high enough for sufficient H_2O and O_2 inputs to achieve complete fuel conversion. The exit reformate composition is based on water–gas-shift equilibrium of H_2, CO, CO_2 and H_2O at the calculated outlet temperature. This approach does not capture the potential for CH_4 in the reformate stream. CH_4 concentrations in ATR reformate have been shown to be below 0.5% for operating pressures up to 3 bar and outlet temperatures of 1000 K or higher at the S/C ratios in this study [10]. A complimentary program with this modeling study has been developing an ATR following an earlier reported design [16] for operating pressures as modeled here, and results have shown similarly low CH_4 outlet concentrations. Such low concentrations of CH_4 will not significantly impact the partial pressure of H_2 through the membrane reactor nor impede H_2 diffusion through the Pd-alloy-membrane, and thus, the CH_4 concentrations in the reformate are assumed negligible and all carbon in the reformate is assumed to be in CO or CO_2.

For the cases presented here, the fuel processor inlet temperature $T_{ref,in}$ is not allowed to increase above 500 °C, assuming sufficient heat input for water and fuel vaporization, with subsequent gas flow preheating. While $T_{ref,in}$ is adequate for all reactor conditions with an exothermic reactant mixture, it is too low for conditions where endothermic steam reforming is the dominant reaction. The current study includes an analysis of the performance trade-offs between varying S/C and O/C ratios, with the sum of these held constant at 2.4 and a mildly exothermic base case of S/C = 1.6 and O/C = 0.8.

The water–gas-shift/Pd-alloy-membrane reactor is modeled with the reformate stream and the sweep stream in counter-flow. The integrated water–gas-shift reaction increases H_2 driving potential along the length of the Pd-alloy-membrane. Furthermore, as gases flow along the length of the reactor, H_2 diffusion across the membrane favors additional H_2 production in the reformate stream to maintain equilibrium. To simulate this effect more accurately, the water–gas-shift reactor is discretized into four segments with local energy balances solved iteratively to determine temperature and mole fraction profiles along the length of the reactor. In the discrete approximation, the water–gas-shift reaction is assumed to reach equilibrium at the entrance to each segment.

The reactor is assumed to be of sufficient size that H_2 diffusion is not limited by mass transfer. Therefore, the amount of hydrogen that diffuses through the membrane is based upon specified H_2 recovery fraction. This represents the ratio of H_2 recovered through the membrane to the sum of H_2 entering in the reformate stream and H_2 produced through water–gas-shift in the membrane reactor. In the present study, membrane H_2 recovery fraction is varied with a baseline case set at 75%. Significantly higher H_2 recovery efficiencies are not considered feasible, because of the loss of H_2 partial pressure difference that serves as a driving potential across the membrane.

2.3.3. Compressor and pump models

The low-pressure-air compressor supplies air to the fuel cell cathode. Inlet conditions are set to ambient, and the outlet pressure is determined to match the cumulative pressure drop through components in the cathode loop. The outlet enthalpy and temperature are determined from an isentropic efficiency, which is determined through cubic polynomials fitted to publicly available data for a rotary vane compressor [17]. These account for variations in pressure ratio and mass flow rate. The required work input is then determined by the enthalpy change through the compressor, plus any heat loss to the ambient. A similar approach is adopted for the high-pressure air compressor and the anode recirculation compressor models, except that isentropic efficiency depends only on pressure ratio.

Power required by the coolant pump, reformer water pump, fuel pump, and sweep steam water pump are determined from the isentropic value divided by a user-specified isentropic efficiency. For the relatively small power demand of the pumps compared to other parasitic loads in the system, isentropic efficiencies are simply set constant at 0.50.

2.3.4. Heat exchanger, fan, and exhaust burner models

The system model includes individual heat exchanger models for the exhaust condenser, low-pressure-air compressor cooler, anode flow condenser, and coolant radiator. These are based on geometry, with corresponding heat transfer and pressure drop correlations, intended for maximum heat rejection in minimal volumes. The burner exhaust condenser and coolant loop radiator are modeled as air-cooled cross-flow heat exchangers, while the air compressor outlet heat exchanger and the anode flow condenser are modeled as counterflow plate heat exchangers. A liquid coolant loop provides cooling, via parallel branches, to each plate heat exchanger and to the fuel cell stack.

For the exhaust condenser, inlet temperature and species mole fraction values for the burner exhaust gas are received from the fuel vaporizer. Inlet conditions for the cooling air are initially set at ambient conditions. The inlet air pressure is subsequently updated after the air-side pressure drop across the heat exchanger is calculated. A target outlet temperature for the system exhaust flow is defined as 10 °C higher than ambient temperature, but not less than 30 °C because of the diminishing benefit in water recovery below this point. The exhaust gas outlet temperature is normally held fixed for given ambient conditions, but may be relaxed as described below. With the burner exhaust gas inlet and outlet conditions specified, the required heat load for the exhaust condenser is defined through an enthalpy balance. The average outlet temperature of the cooling air is then adjusted iteratively until the heat removal capacity of the heat exchanger matches the required heat load. As the air outlet temperature is adjusted, it varies the heat removal capacity of the exhaust condenser by changing the log mean temperature difference across the heat exchanger. Adjusting the air outlet temperature also determines the required air mass flow rate to satisfy an enthalpy balance between burner exhaust gas and the cooling air. This affects the friction factor and, in the case of turbulent conditions, the heat transfer coefficient through changes in flow velocity and Reynolds number. To prevent second-law violations, the solver is also constrained to keep the average air outlet temperature less than the burner exhaust inlet temperature. Similarly, the burner exhaust outlet temperature must remain above the inlet temperature of the cooling air.

To prevent uncontrolled growth in condenser fan power under high heat load conditions, velocity of the cooling air is constrained to a maximum of 3 m s^{-1}. When this constraint is active, the model relaxes burner exhaust gas outlet temperature to the extent needed to match heat removal from the gas with available heat exchanger capacity.

Constant wall temperature conditions are assumed for the purpose of determining the convection coefficient under laminar conditions. For turbulent flow conditions, the friction factor inside the tubes is determined based on the relationship by Petukhov [18] and the internal tube heat transfer coefficient is determined using Gnielinski's correlation [19] for Nusselt number. In the transition region between laminar and turbulent conditions, the friction factor and convection coefficient are modeled as varying linearly between their high-end laminar and low-end turbulent values.

The pressure drop of the cooling air flow is determined from friction factor based on the correlation of Chang et al. [20], which was found to predict reasonable values of friction factor over the range of conditions modeled. For the air-side heat transfer coefficient, the model determines the Nusselt number from a Chilton–Colburn factor for a radiator with louvered fins using the correlation found in Chang et al. [21] for a Reynolds number (Re_{Lp}) between the limits of 100 and 3000 which falls within the range of conditions modeled in this study. For $Re_{Lp} < 100$, the model calculates the convection coefficient based on a constant Nusselt number, as evaluated at the lower Re_{Lp} limit.

The required fan power is determined by the enthalpy difference between ambient air entering the fan and air exiting the fan at a sufficient pressure to match the pressure drop across the exhaust condenser. The exit enthalpy is calculated based on an isentropic enthalpy increase divided by isentropic fan efficiency. For given combinations of flow rate and pressure increase, the isentropic efficiency is determined through a map based on characteristic curves measured for an axial fan. Flow rates and pressure ratios in the map are expressed relative to their maximum values, such that the efficiency map can be scaled to varying fan sizes. Because of accuracy limitations of the efficiency map at air velocities less than 0.12 m s^{-1}, fan power is calculated as scaling with the cube of air velocity under these conditions.

The coolant loop radiator receives the coolant inlet temperature and species mole fraction values from the coolant pump. The radiator fan speed remains bounded under all conditions tested with no active constraint on maximum air velocity, and therefore, no provision for relaxing the coolant outlet temperature is needed. Otherwise, calculations in the coolant loop radiator are handled similarly to those in the exhaust condenser.

The anode flow condenser transfers heat from hot anode gas to the coolant loop. The friction factor and the turbulent-range heat transfer coefficient for both flows are calculated as they are for the burner exhaust flow in the exhaust condenser. For laminar conditions, the heat transfer coefficient for both flows is based on constant surface temperature Nusselt numbers determined by Kays and Crawford [22] over a range of channel aspect ratios. The coolant outlet temperature is limited to a maximum of 90 °C to prevent boiling. This has the effect of enforcing a minimum coolant mass flow rate through the heat exchanger.

The anode flow condenser is sized for operation at design conditions that represent the most demanding of the anticipated operating conditions. Under less severe conditions, the required heat load is smaller, which results in a lower mass flow rate and greater temperature rise of the coolant. When the heat load decreases to the point that the coolant reaches its maximum permitted outlet temperature, the coolant mass flow rate cannot be reduced any more. If the heat load is decreased further, the anode flow outlet temperature must drop below its set target value in order for enthalpy change in the anode flow to match the heat removal capacity of the anode flow condenser. The model detects that this condition has occurred when the energy balance residual for calculating the coolant outlet temperature iterations fails to achieve convergence with all imposed temperature constraints. In this case, the model allows the anode flow outlet temperature to be adjusted as a design variable and repeats the iterative calculation of coolant outlet temperature.

If the required anode flow enthalpy change (i.e., heat load) continues to drop, the anode flow outlet temperature is allowed to decrease until it reaches within 0.01 °C of the coolant inlet temperature. If the required heat transfer to the coolant decreases beyond this point, it becomes insensitive to the heat exchanger channel length. Under such a condition, the required enthalpy change of the anode flow can take place in less than fixed length of the heat exchanger channels. The model responds by relaxing the channel length and re-calculating the heat exchanger enthalpy balance. The channel length at which the solver converges represents the

Table 1
Critical baseline system parameters

Parameter	Value
Ambient conditions	
Temperature, T_{amb} (K)	303.15
Relative humidity, ϕ_{amb}	50%
Fuel cell conditions and properties	
Operating temperature, T_{cell} (K)	338.15
Pressure drop across stack at 1 A cm^{-2} current density (bar)	0.5
Stoichiometric ratio of cathode air flow	1.8
Stoichiometric ratio of anode H_2 flow	1.5
Fraction of water produced in fuel cell transported to anode	15%
Number of cells per stack	25
Stack membrane area per cell (cm^2)	487
Current density at 8000 W gross power, i_{ref} (A cm^{-2})	1.0
Fuel reformer conditions	
Inlet oxygen to carbon (O/C) ratio	0.8
Inlet steam to carbon (S/C) ratio	1.6
Maximum inlet temperature, $T_{ref,in,max}$ (K)	773
Minimum pre-heater approach temperature (K)	20
Minimum approach temperature for steam generator (K)	40
Maximum temperature out of steam generator (K)	470
Water–gas-shift membrane reactor conditions:	
Differential pressure across membrane (bar)	6.0
Sweep steam to H_2 ratio in the membrane separator	0.20
Membrane reactor H_2 recovery fraction	75%
Temperature out of the sweep steam generator (K)	450
Balance-of-plant conditions:	
Radiator coolant outlet temperature (K)	333.15
Burner exhaust condenser temperature difference (K)	10
Electric inverter efficiency	93%
Electric motor efficiency	90%

fraction of the channel length actually needed to accomplish the required enthalpy change.

No condensation takes place in the air compressor outlet heat exchanger, but it is otherwise similar to the anode flow condenser. Both heat exchangers use the same modeling approach.

Exhaust gas from the retentate burner provides heat inputs to the reformer steam generator, fuel vaporizer, and reformer pre-heater. Each of these is represented by a zero-order model that determines the burner exhaust outlet temperature iteratively to satisfy an enthalpy balance. Maximum allowable outlet temperatures are specified for the flows being heated. A zero-order model also represents heat rejection from the fuel cell stack to the coolant loop. In this model, the coolant outlet temperature is limited to 80 °C in order to prevent excessive stack temperature and the accompanying risk of Nafion membrane dryout.

3. Results

3.1. Baseline system performance

Results from the system model identify how critical parameters influence both overall efficiency and water balance for the integrated power plant. Baseline conditions for user-specified variables used in the current system simulations are provided in Table 1. For a given simulation condition, the overall system efficiency η_{th} is found from Eq. (1) which shows η_{th} in terms of fuel cell power out, parasitic loads, $\dot{W}_{lost}$, and enthalpy input of the hydrocarbon fuel in $\dot{m}_{HC,in} h_{HC,comb}$.

$$\eta_{th} = \frac{\dot{W}_{net}}{\dot{Q}_{HC}} = \frac{n_{cells} A_{cell} iV_{cell} - \dot{W}_{lost}}{\dot{m}_{HC,in} h_{HC,comb}} \quad (1)$$

η_{th} can be broken up into three components: the combined efficiency of the fuel processor and Pd-alloy-membrane η_{FP}, the efficiency of the fuel cell itself η_{FC}, and the efficiency of the balance-of-plant η_{BOP}. These three sub-system efficiencies are shown in each expression in parenthesis in the right-hand-side of the following equation:

$$\eta_{th} = \eta_{FP}\eta_{FC}\eta_{BOP} = \left(\frac{\dot{m}_{H_2,mem} h_{H_2,comb}}{\dot{m}_{HC,in} h_{HC,comb}}\right)\left(\frac{n_{cells} A_{cell} iV_{cell}}{\dot{m}_{H_2,mem} h_{H_2,comb}}\right) \times \left(\frac{n_{cells} A_{cell} iV_{cell} - \dot{W}_{lost}}{n_{cells} A_{cell} iV_{cell}}\right) \quad (2)$$

η_{FP} is proportional to the membrane recovery fraction which in this model is set constant, and variations in η_{FP} are primarily due to changes in the S/C and O/C ratios of the fuel processor. η_{FC} is proportional to V_{cell} because for the recirculated anode flow at steady state, i will be proportional to $\dot{m}_{H_2,mem}$. Thus, as V_{cell} drops with higher i and higher stack power densities, η_{FC} will tend to fall off, and this decrease in η_{FC} with increased power can more than offset improved efficiencies in the compressors as they approach their capacity with increased system power. This trend is illustrated in Table 2 which shows key system performance metrics for baseline conditions at half- and full-load. Fig. 2 shows η_{th} as a function of $\dot{W}_{net}$ for 3 different T_{amb}: 10, 30, and 50 °C. For all three T_{amb}, η_{th} decreases as $\dot{W}_{net}$ rises above 1500 W. This is due to the drop in η_{FC}. The decrease in η_{th} at low power densities is due to the large decrease in η_{BOP} caused by relative increases in the compressor and fan loads $\dot{W}_{lost}$ to fuel cell power output $\dot{W}_{gross}$ as $\dot{W}_{net}$ decreases below 1500 W as illustrated for all T_{amb} in Fig. 2.

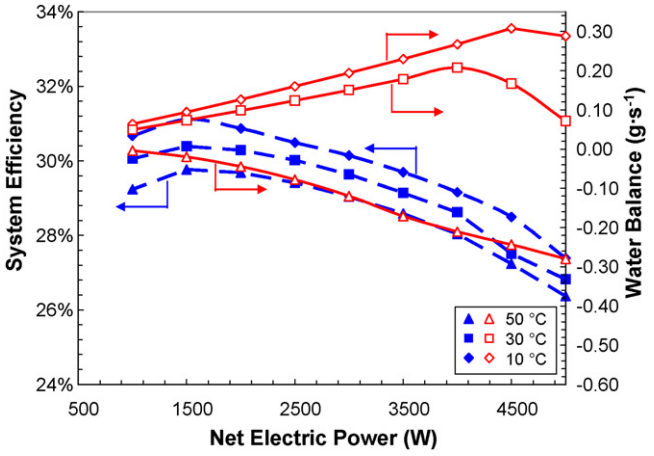

Fig. 2. Overall system efficiency and total water balance (in g s^{-1} accumulated) as functions of net electric power for the liquid-fueled PEM fuel cell system at baseline conditions (see Table 1) at three different ambient temperatures. Numbers on top of bars indicate T_{amb}.

Table 2
Key system states and outputs for two $\dot{W}_{net}$ baseline conditions from Table 1

Parameter	Value	
$\dot{W}_{net}$ (W)	2500	5000
Overall system efficiency, η_{th}	0.301	0.268
Individual cell voltage (V)	0.75	0.70
Gross power demand, $\dot{W}_{gross}$ (W)	3242.5	6721.0
Net water balance (g s^{-1})	0.124	0.071
Reformer outlet temperature, $T_{ref,out}$ (K)	952.7	975.7
WGS membrane reactor conditions		
Inlet reformate temperature, $T_{WGS,ref,in}$ (K)	822.2	870.2
Outlet reformate temperature, $T_{WGS,ref,out}$ (K)	859.8	917.1
Outlet sweep-stream temperature, $T_{WGS,sweep,out}$ (K)	889.9	935.0
Inlet reformate pressure, $P_{WGS,ref,in}$ (bar)	7.31	7.53
Inlet sweep-stream pressure, $P_{WGS,sweep,in}$ (bar)	1.31	1.53

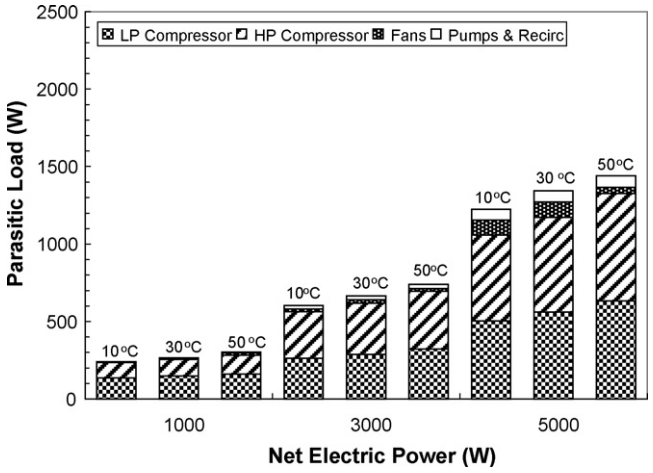

Fig. 3. Parasitic loads for LP and HP compressors, cooling fans, and liquid pumps for the liquid-fueled PEM fuel cell system at baseline conditions (see Table 1) at three different ambient T_{amb} and $\dot{W}_{net}$.

The trends in η_{th} as a function of $\dot{W}_{net}$ are consistent at all 3 T_{amb}, but also as shown in Fig. 2, there is a monotonic decrease in η_{th} with increasing T_{amb}. This is due to an increase in $\dot{W}_{lost}$ due to compressor loads rising with T_{amb}. The drop in η_{th} is approximately 2% points for each 20 °C rise in temperature, and this result shows the importance of stating system efficiency values at a given T_{amb}.

For a small-scale fuel cell generator, changes in total parasitic loads $\dot{W}_{lost}$ (from the balance-of-plant components and the dc to ac inverter) with operating conditions determines how η_{BOP} influences the overall η_{th}. Fig. 3 shows changes with $\dot{W}_{net}$ in parasitic loads at three T_{amb} (for the otherwise baseline conditions). The parasitic loads are broken out into groups of components—the LP compressor for the cathode flow, HP compressor for the reformer air supply, cooling fans for the fuel cell radiator and exhaust condenser, and pumps (including all liquid pumps and the anode recirculation compressor). At the baseline reformer conditions (S/C = 1.6 and O/C = 0.8), the LP and HP compressors are the chief contributors to the parasitic power demand. Both compressor demands increase similarly with $\dot{W}_{net}$ and T_{amb}. The total power for the fans $\dot{W}_{fan}$ also increases with $\dot{W}_{net}$. Because of the low required fan speeds at less rigorous operating conditions, the $\dot{W}_{fan}$ dependencies only becomes significant for $\dot{W}_{net} \geq 3000$ W. With respect to T_{amb}, the radiator fan power demand increases with T_{amb} because of the larger coolant loop heat load coming from the fuel cell. However, the power demand of the exhaust condenser fan decreases at higher T_{amb} because of the smaller heat load due to less condensation. This variation however does not significantly impact the trends in total $\dot{W}_{lost}$ due to the fact that fan power at these conditions is still relatively small.

In addition to η_{th}, overall system water balance is a critical measure of the system performance. Water balance is measured by the difference between the water collected from the exhaust condenser and the anode inlet heat exchanger (condenser) and the amount of water demanded by the fuel processor and the sweep steam for the low-pressure side of the Pd-alloy-membrane. As discussed earlier and illustrated in Fig. 1, there are really two water balances: (1) a clean water loop involving the anode inlet condenser, the fuel cell, and the sweep-steam generator and (2) a fuel-processor-water loop involving the autothermal reformer and the exhaust condenser. Excess from the clean water loop can be supplied to the fuel processor water loop, and thus the total water balance will be presented as a single value in these results. However, because the anode recirculation loop is essentially closed except for flow across the fuel cell Nafion membrane, water recovery from this loop is near complete and independent of variations in T_{amb}. Thus, water recovery from the burner exhaust condenser is most critical in determining overall water balance in the system.

Fig. 2 also shows the variation of net system water balance with $\dot{W}_{net}$ for T_{amb} of 10, 30, and 50 °C. As is consistent with other system-level studies [10], the net water balance was most sensitive to the outlet temperature of the exhaust condenser T_{exh}. For the current study, T_{exh} is set to T_{amb} + 10 °C by varying the fan power except for conditions (at high $\dot{W}_{net}$ and lower T_{amb} which leads to more condensation) when the fan flow rate reaches its limit at a velocity of 3 m s^{-1} across the condenser face. For the range of conditions where T_{exh} follows T_{amb} + 10 °C, the net water balance follows a near linear relationship with $\dot{W}_{net}$ as illustrated in Fig. 2. Such linear behavior implies that for most T_{amb}. The net water balance grows either more negative or positive with $\dot{W}_{net}$ for a given T_{amb}. For the cases in Fig. 2, water balance remains positive for T_{amb} at 10 and 30 °C and negative for 50 °C. At high $\dot{W}_{net}$, the fan hits its flow rate limits and T_{exh} rises above its desired valued for all T_{amb} < 50 °C. The effect of this fan power limit on the water balance is shown in Fig. 2 where the net water balance drops below its linear behavior at the high $\dot{W}_{net}$ for 10 and 30 °C.

At a given T_{amb}, the overall system water balance magnitude increases with respect to $\dot{W}_{net}$ until the exhaust condenser airflow reaches its maximum allowable velocity. Beyond this point, the exhaust condenser cannot recover additional water as the system demand for water increases. Thus, further increases in $\dot{W}_{net}$ result in net decrease in water balance. For T_{amb} equal to 50 °C, the current system does not meet water balance at any load conditions. In this case, insufficient water recovery in the exhaust condenser is due to the high T_{exh}, rather than the air velocity constraint, limiting the extent to which the burner gas cools and condenses. Fig. 4 illustrates the strong dependence of overall system water balance on T_{amb} for half and full power conditions. Fig. 4 also indicates the variation in η_{th} with T_{amb} and shows a drop of 2–3% points when T_{amb} rises from 10 to 50 °C.

For the current system configuration, the water balance is positive for T_{amb} approaching 40 °C at full power. Near 40 °C, the water balance shifts from positive to negative water balances as $\dot{W}_{net}$ increases due to the exhaust fan reaching its flow rate limits before T_{exh} cools to its desired value of T_{amb} + 10 °C. For T_{amb} > 44 °C, the water balance becomes negative for all values of $\dot{W}_{net}$ for the given configuration. The difference between T_{exh} and T_{amb} can be reduced at the expense of condenser size and fan power to maintain positive water balances at higher T_{amb}. Also, it should be noted that

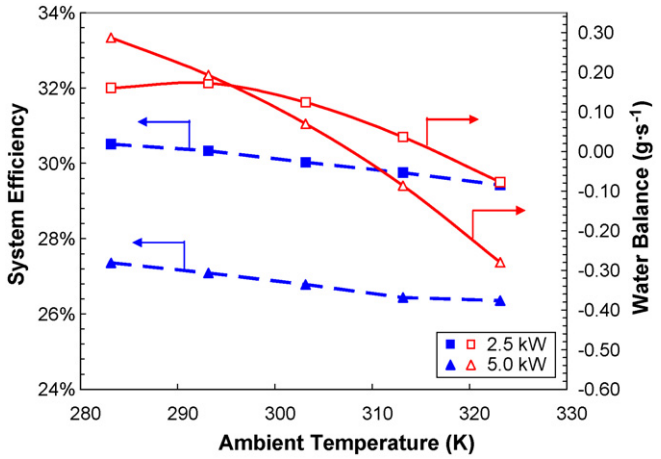

Fig. 4. Overall system efficiency and total net water balance as functions of ambient temperature for full-load and half-load conditions.

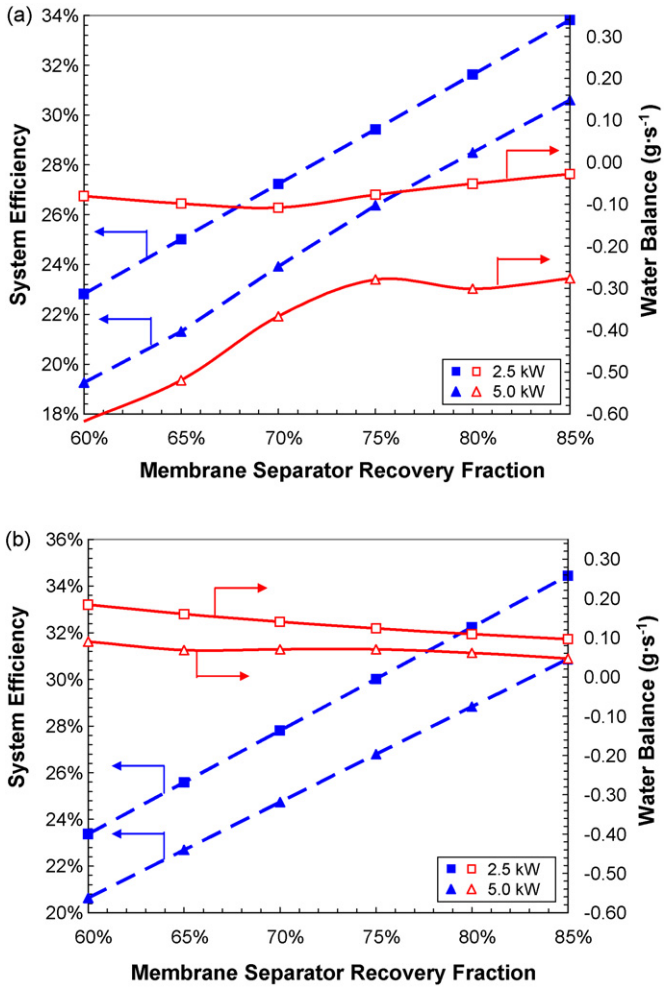

Fig. 5. (a) Overall system efficiency and total net water balance as functions of H_2 recovery fraction of the Pd-alloy-membrane for full-load and half-load conditions: (a) at 30 °C ambient and (b) at 50 °C ambient.

increases in the reformer O/C ratio relative to S/C ratio can raise the T_{amb} threshold for maintaining positive water balance. Finally, fuel cell V_{cell}, which is a function of stack size and polarization curves, affect water balance, since the non-linearity in the water balance with respect to power changes is due mainly to the non-linear change in the stack current with power as discussed above.

3.2. Effects of fuel processor and H_2 purification on system performance

For this fuel cell generator with a liquid-fuel reformer and a Pd-alloy-membrane purifier, η_{th} is very sensitive to both the fuel cell operation voltage (through η_{FC}) and the membrane H_2 recovery fraction (through η_{FP}). The membrane recovery fraction is defined by the fraction of total H_2 that crosses over to the low-pressure, purified side of the membrane. As η_{FP} decreases, a greater total H_2 flow is needed from the fuel processor to supply the same H_2 flow to the fuel cell stack. Increased fuel consumption requires increased air and water flow rates to the fuel processor, along with greater parasitic power consumption. Increases in membrane recovery fraction improve η_{th} as indicated in Fig. 5a for T_{amb} = 30 °C and Fig. 5b for T_{amb} = 50 °C. On the other hand, there is improvement in the water balance as membrane recovery fraction decreases. This is due to the greater availability of H_2 in the retentate flow and thus H_2O in the burner exhaust.

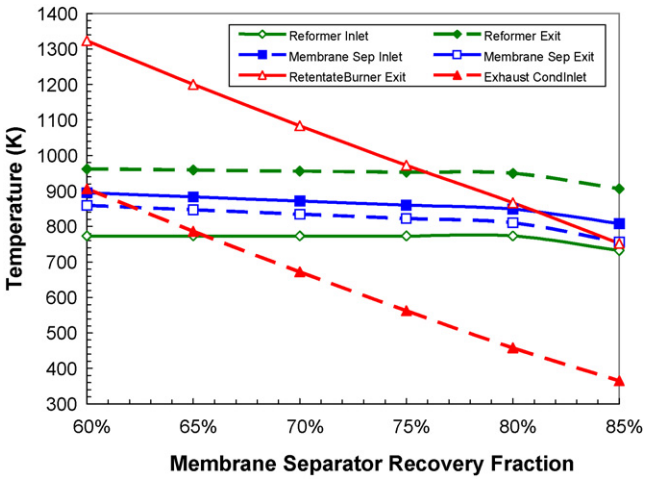

Fig. 6. Critical system temperatures as functions of H_2 recovery fraction of the Pd-alloy-membrane for $\dot{W}_{net}$ = 2.5 kW at T_{amb} = 30 °C.

The recovery fraction of the Pd-alloy-membrane not only impacts the system efficiency, but also the operating temperatures of many of the system's components. Fig. 6 illustrates the effect of recovery fraction on a range of critical high T locations associated with the fuel processor and the exhaust burner. For lower membrane recovery fractions, the increased H_2 content in the retentate flow results in a higher outlet temperature from the exhaust burner. Since the amount of heat that can be recovered from the system is limited, any extra heat must be rejected to the ambient, which significantly reduces η_{th}. This drop in η_{th} with reduced membrane recovery fractions is exacerbated by higher T_{amb}. At lower T_{amb} as shown in Fig. 5a, sufficient water can be recovered from the burner exhaust condenser to achieve a net positive water balance across a range of membrane recovery fractions. By contrast, at high T_{amb} (50 °C) as illustrated in Fig. 5b, the higher T_{exh} limits the water recovery and does not allow for improved water balances with reduced membrane recovery fractions. Thus, no benefits can be achieved by reducing membrane recovery fractions at high T_{amb} operation. The trends shown in Fig. 5a and b indicate that the design and control of the water–gas-shift/membrane reactor and H_2 purifier is central to achieving an efficient and operable generator when it is chosen as part of the fuel processing sub-system.

Additional simulations represented in Fig. 7a and b investigate the impact of varying the stoichiometry of the liquid-fuel reformer, while keeping the sum of S/C and O/C fixed at 2.4. This fixed sum of S/C and O/C is prescribed such that there is adequate oxygen content in the feed to avoid coking in the reformer [23]. A sum of S/C and O/C below this point increases the risk of carbon deposition on the reformer catalyst, thereby degrading performance. Increasing S/C and decreasing O/C significantly improves η_{th}. This is due, in part, to the greater H_2 yield from steam reforming compared to partial oxidation and thus a rise in η_{FP}. However, in addition, reducing O/C also reduces the flow demand from the HP compressor for the fuel processor air. Reducing the high power demand of the HP compressor (relative to the liquid pump for the reformer steam supply) increases η_{BOP} which further contributes to the rise in the overall η_{th}. Comparing Fig. 7a and b shows that the influence of high T_{amb} negatively impacts both η_{th} and overall water balance at all values of S/C although the impacts are less severe at half-load than at full-load.

The benefits in η_{th} with increasing S/C are not offset by drops by overall system water balance as indicated in Fig. 7a and b, and thus, it would appear that S/C should be increased as high as possible to improve system performance. However, system

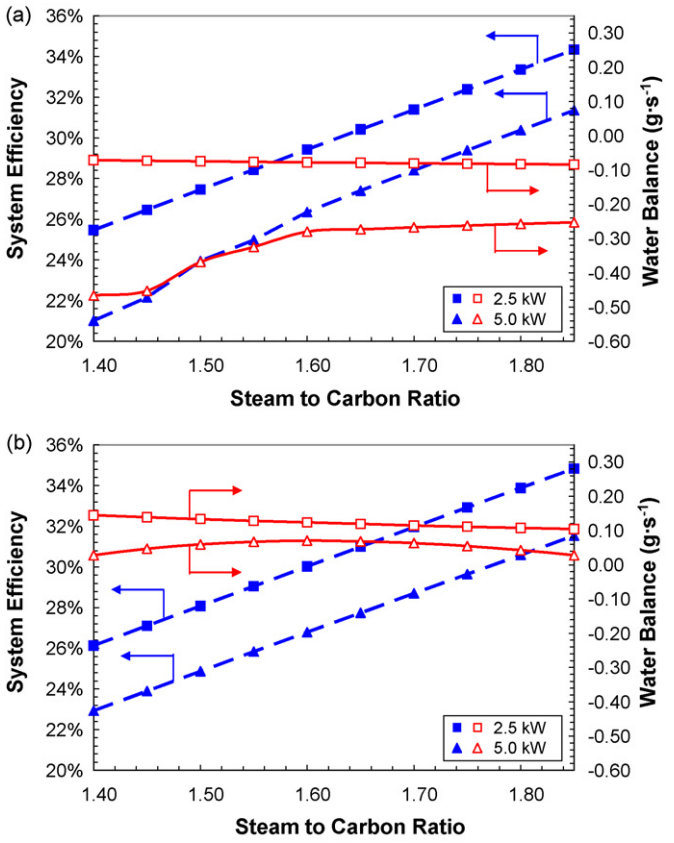

Fig. 7. System efficiency and total water balance versus fuel reformer S/C (where fuel reformer O/C is set to 2.4 – S/C) for full-load and half-load conditions (a) at T_{amb} = 30 °C and (b) at T_{amb} = 50 °C.

limitations, including the challenge and expense (in terms of system size and volume) of providing low-cost heat to the reformer as the process becomes increasingly endothermic, make it beneficial to provide some degree of oxygen to the fuel processor to increase the exothermic nature of the fuel reformer reactions. Fig. 8 shows how variations in reformer S/C, with corresponding decreases in O/C impact the critical high-temperature locations associated with the reformer, WGS/membrane reactor, and retentate burner. In

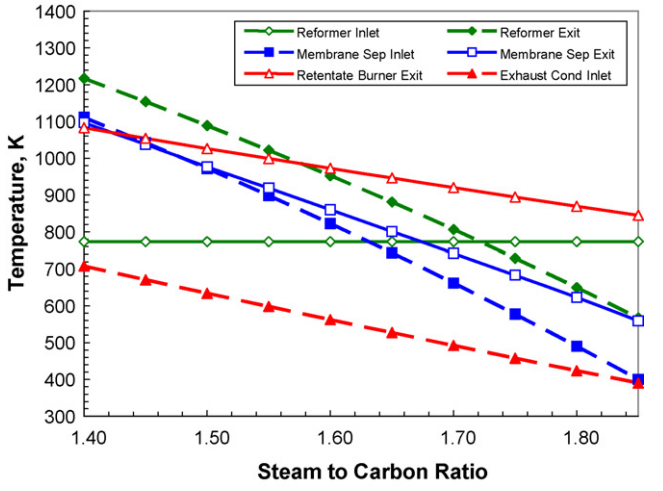

Fig. 8. Critical system temperatures as functions of S/C (where fuel reformer O/C is set to 2.4 – S/C) for $\dot{W}_{net}$ = 2.5 kW at T_{amb} = 30 °C.

Table 3
Breakdown of system efficiency at full and half power for a range of S/C and T_{amb}

S/C	T_{amb} (K)	$\dot{W}_{net}$ (kW)	η_{FP}	η_{FC}	η_{BOP}	η_{th}
1.4	303.15	2.5	0.589	0.598	0.743	0.262
		5.0	0.589	0.550	0.707	0.229
	323.15	2.5	0.589	0.597	0.725	0.255
		5.0	0.589	0.542	0.657	0.210
1.6	303.15	2.5	0.649	0.600	0.772	0.301
		5.0	0.649	0.555	0.743	0.268
	323.15	2.5	0.649	0.599	0.758	0.295
		5.0	0.649	0.554	0.733	0.264
1.8	303.15	2.5	0.710	0.601	0.796	0.339
		5.0	0.710	0.559	0.772	0.306
	323.15	2.5	0.710	0.600	0.786	0.335
		5.0	0.710	0.558	0.767	0.304

general, the increasing endothermic nature of the reformer with increasing S/C drops the temperatures of the autothermal reformer and puts a greater requirement on heat recirculation from burner exhaust.

For autothermal reformers of liquid hydrocarbons fuels, studies have shown that near 100% conversion of the hydrocarbons and pyrolysis intermediates requires reactor temperatures above 700 °C [24]. As S/C increases much above the baseline value of 1.6 (with O/C decreasing from its baseline of 0.8), the existing configuration cannot sustain such high temperatures. While clever reactor design with sequential injection or increased heat recirculation may be used to expand the range of S/C available for the system, assessing the feasibility of such approaches is outside the scope of this study.

4. Discussion

Table 3 documents values of η_{FP}, η_{FC}, and η_{BOP} for a range of operating conditions. For the range of operating conditions in Table 3, trends in η_{FC} and η_{BOP} follow each other with changes in S/C, T_{amb}, and $\dot{W}_{net}$. Since decreases in η_{FC} result in greater system flow rate requirements, trends in η_{FC} are mirrored in the trends of η_{BOP} at these operating conditions. However, for $\dot{W}_{net}$ below 1500 W, the diminished efficiency of the LP compressor at low flow rates results in an opposing trend between η_{FC} and η_{BOP}. There are also strong trade-offs between fuel cell stack size and η_{FC}, and between stack size and η_{BOP}. Therefore, η_{FC} and η_{BOP} can be significantly influenced for a given application through fuel cell stack size, which may often be dictated by cost targets for a given generator application. For a given application, the preferred stack size is a function of the V_{cell} versus i curve and $\dot{W}_{net}$ demand for a given condition. An increase in fuel cell size not only improves η_{FC} by increasing V_{cell} with a lower i but also increases η_{BOP} by decreasing $\dot{W}_{lost}$ from the balance-of-plant due to the lower flow rates both for the cathode and fuel processor with the higher V_{cell} at a given $\dot{W}_{net}$. Thus, for applications where cost and perhaps system size is not as critical as η_{th}, large fuel cell stacks may prove to be a viable approach for maximizing system efficiency.

Identifying other areas for improving overall system efficiency and water balance is one of the underlying goals in establishing the simulation tool in this study. It is clear from the complex behavior of the system water balance and η_{th} with respect to $\dot{W}_{net}$ and to a lesser extent T_{amb}, improving system performance requires an understanding of the range of operating conditions and load profiles for a given application. Furthermore, maintaining as possible a positive or minimally negative instantaneous water balance for a stand-alone generator application may lead to changes in fuel processor stoichiometry or membrane effectiveness that can greatly influence system performance.

Clearly from Fig. 7, one of the key ways to improve η_{th} primarily through raising η_{FC} is increasing fuel processor S/C, but this can only be done if there is adequate heat recirculation or reactor design to ensure near equilibrium fuel reformer outlets. Another means of improving performance is to increase η_{BOP} by lowering parasitic loads. From looking at Fig. 3, it is clear that the two compressors provide the largest fraction of $\dot{W}_{lost}$. The cathode LP compressor parasitic load can be reduced by running a lower-pressure drop stack, or by developing compressors with improved isentropic efficiencies at the reduced $\dot{W}_{net}$ conditions. The HP compressor load may be dramatically reduced by finding a lower pressure H_2 purification process. This may be achieved by ultra-thin (<5 μm) Pd-alloy-membranes, which may not require the 6.0 bar differential total pressure across the membrane and thereby reduce the contribution to $\dot{W}_{lost}$ by the HP compressor. Another means of reducing the HP compressor load is to use a preferential CO oxidation (PROx) reactor (as proposed in other studies [8,10,25] to replace a Pd-alloy-membrane for H_2 purification. However, PROx reactors add penalties by adding additional air flow requirements (for the oxidation stream) and by reducing the fuel cell stack performance with reduced H_2 anode concentrations and non-zero CO anode concentrations. Because of the concentrations of CO_2, CO, and N_2 in the reformate, PROx-based systems are not amenable to anode recirculation. While such systems may be capable of utilizing H_2 exhausted from the anode for heat generation or water recovery, they cannot utilize it in the fuel cell stack. Studying the trade-offs between lowering the pressure of the fuel reformer and reducing the fuel cell stack performance with a PROx reactor is left for a further study.

While the LP and HP compressors are the chief parasitic loads, the cooling system also demands a significant power at high $\dot{W}_{net}$, and improvements in η_{BOP} may be achieved through optimized heat exchanger design. Pressure drops across the exhaust heat exchangers which determine fan parasitic loads are highly nonlinear (approximately cubic) with respect to air flow rates. This in part causes the increased power demand of both cooling fans which contributes to the consistent drop in η_{BOP} with increasing $\dot{W}_{net}$. At high T_{amb} however, parasitic loads for system cooling are somewhat offset by reduced heat transfer requirements in the exhaust condenser due to lower condensation rates. In fact, if the condenser approach temperature is held constant, the heat removal to condense large amounts of water in the exhaust increases with lower T_{amb} (particularly $\leq$20 °C). This increases fan power for the condenser for these lower T_{amb} as well. This provides an additional opportunity for higher η_{BOP} through a complex fan power control algorithm to let the $T_{exh} - T_{amb}$ difference float with existing operating conditions in order to optimize fan power while ensuring positive for water balance. Resulting improvements in η_{BOP} and thus, η_{th} through improved fan power control will not be as significant as increases from reducing the compressor loads.

5. Conclusion

The system analysis presented in this study can effectively be used to assess the performance of a liquid-fuel-powered PEM fuel cell system. The tool provides a qualitative basis for understanding the sensitivity of overall η_{th} and system water balance to the different component parameters in the fuel cell stack, the fuel processor and H_2 purifier, and the remaining balance-of-plant. The system model is also critical for identifying operating conditions for internal components as a function of global operation parameters such as fuel process S/C and O/C and fuel cell stack V_{cell}. Thus, the model can assess which approaches for improving η_{th} and system water balance will maintain components in feasible operating temperatures and pressures. The quantitative results of the simulations will thus aid in designing components such as the fuel processor, heat exchangers, and balance-of-plant by providing the designer with the range of possible operating conditions.

The current study indicates that stand-alone operation of a PEM fuel cell generator with a fuel processor and a liquid hydrocarbon fuel source is feasible, subject to constraints on ambient conditions and operating parameters. For the system detailed in the present study, the overall system performance is highly sensitive to fuel cell stack V_{cell}, H_2 purifier recovery fraction, and fuel processor S/C and O/C ratios. Generator performance also varies with the environmental variable T_{amb}. Isentropic efficiencies, particularly of compressors for air supply and fans for cooling along with their necessary discharge pressures, dominate the losses in η_{th} due to balance-of-plant. The simulations reveal a trade-off at higher T_{amb} in performance between η_{th} and net water balance. For the system configuration in the current study, water balance for the system configuration is maintained for T_{amb} up to 35 °C at full power demand and up to 44 °C at 50% power demand. Maximizing η_{th} favors running the system with the highest fuel processor S/C that still allows sufficient internal reformer temperatures to sustain high fuel conversion in the fuel processor and the exhaust burner. The revealed design trade-offs show the importance of putting even simple component models into their system context to understand how they influence the system performance as well as how the system context influences their design and performance.

Acknowledgment

The authors acknowledge the support of this work from the Army Research Laboratory for under contract number W911QX-05-C-0107 (Dr. Deryn Chu, program manager).

References

[1] T. Berning, N. Djilali, Journal of the Electrochemical Society 150 (2003) A1589–A1598.
[2] G.H. Guvelioglu, H.G. Stenger, Journal of Power Sources 147 (2005) 95–106.
[3] G.Y. Lin, T. Van Nguyen, Journal of the Electrochemical Society 153 (2006) A372–A382.
[4] B.R. Sivertsen, N. Djilali, Journal of Power Sources 141 (2005) 65–78.
[5] S. Um, C.Y. Wang, Journal of Power Sources 156 (2006) 211–223.
[6] S.R. Deshmukh, D.G. Vlachos, Industrial and Engineering Chemistry Research 44 (2005) 4982–4992.
[7] S. Tischer, O. Deutschmann, Catalysis Today 105 (2005) 407–413.
[8] S. Ahmed, J. Kopasz, R. Kumar, M. Krumpelt, Journal of Power Sources 112 (2002) 519–530.
[9] R.M. Biesheuvel, G.J. Kramer, Journal of Power Sources 138 (2004) 156–161.
[10] E.D. Doss, R. Kumar, R.K. Ahluwalia, M. Krumpelt, Journal of Power Sources 102 (2001) 1–15.
[11] J.R. Lattner, M.P. Harold, International Journal of Hydrogen Energy 29 (2004) 393–417.
[12] R.K. Ahluwalia, E.D. Doss, R. Kumar, Journal of Power Sources 117 (2003) 45–60.
[13] P. Berg, K. Promislow, J. St Pierre, J. Stumper, B. Wetton, Journal of the Electrochemical Society 151 (2004) A341–A353.
[14] R.K. Ahluwalia, X. Wang, Journal of Power Sources 171 (2007) 63–71.
[15] C.M. Garcia-Salcedo, T.A. Brabbs, B.J. McBride, Experimental verification of the thermodynamic properties for a jet-A fuel, NASA Tech Report, #88-C-014, 1988.
[16] S. Roychoudhury, M. Lyubovsky, D. Walsh, D. Chu, E. Kallio, Journal of Power Sources 160 (2006) 510–513.
[17] Vairex, in, Vol. ed.)êds.), VV-1020 Compressor Map, http://www.vairex.com/products/vv_1020.html#, 2005.
[18] B.S. Petukhov, Advances in Heat Transfer 6 (1970) 503–534.
[19] V. Gnielinski, International Chemical Engineering 16 (1976) 359–368.
[20] Y.-J. Chang, C.-C. Wang, W.-R. Chang, ASHRAE Transactions 100 (1994) 643–652.
[21] Y.-J. Chang, C.-C. Wang, International Journal of Heat and Mass Transfer 40 (1997) 533–544.
[22] W.M. Kays, M.E. Crawford, Convective Heat and Mass Transfer, 3rd ed., McGraw-Hill, New York, 1993.
[23] K. Sasaki, K. Watanabe, Y. Teraoka, Journal of the Electrochemical Society 151 (2004) A965–A970.
[24] I. Kang, J. Bae, G. Bae, Journal of Power Sources 163 (2006) 538–546.
[25] M.J. Castaldi, F. Barrai, Catalysis Today 129 (2007) 397–406.